Single-pulse and profile-variability study of PSR J1022+1001

K. Liu,[1,2,3]★ R. Karuppusamy,[3] K. J. Lee,[3] B. W. Stappers,[4] M. Kramer,[3,4]
R. Smits,[5] M. B. Purver,[4] G. H. Janssen[4,5] and D. Perrodin[6]

[1]*Station de Radioastronomie de Nançay, Observatoire de Paris, CNRS/INSU, F-18330 Nançay, France*
[2]*Laboratoire de Physique et Chimie de l'Environnement et de l'Espace (LPC2E), CNRS-Université d'Orléans, F-45071 Orléans Cedex 02, France*
[3]*Max-Planck-Institut für Radioastronomie, Auf dem Hügel 69, D-53121 Bonn, Germany*
[4]*University of Manchester, Jodrell Bank Centre of Astrophysics, Alan Turing Building, Manchester M13 9PL*
[5]*ASTRON, Oudehoogeveensedijk 4, Dwingeloo, 7991PD, the Netherlands*
[6]*INAF – Osservatorio Astronomico di Cagliari, Via della Scienza 5, I-09047 Selargius (CA), Italy*

ABSTRACT

Millisecond pulsars (MSPs) are known as highly stable celestial clocks. Nevertheless, recent studies have revealed the unstable nature of their integrated pulse profiles, which may limit the achievable pulsar timing precision. In this article, we present a case study on the pulse-profile variability of PSR J1022+1001. We have detected approximately 14 000 subpulses (components of single pulses) in 35-h long observations, mostly located in the trailing component of the integrated profile. Their flux densities and fractional polarization suggest that they represent the bright end of the energy distribution in ordinary emission mode and are not giant pulses. The occurrence of subpulses in the leading and trailing components of the integrated profile is shown to be correlated. For subpulses from the latter, a preferred pulse width of approximately 0.25 ms has been found. Using simultaneous observations from the Effelsberg 100-m telescope and the Westerbork Synthesis Radio Telescope, we have found that the integrated profile varies on a time-scale of a few tens of minutes. We show that improper polarization calibration and diffractive scintillation cannot be the sole reason for the observed instability. In addition, we demonstrate that timing residuals generated from averages of the detected subpulses are dominated by phase jitter and we place an upper limit of ∼700 ns on jitter noise, based on continuous 1-min integrations.

Key words: methods: data analysis – pulsars: individual: PSR J1022+1001.

1 INTRODUCTION

Rotation-powered pulsars have been shown to be stable celestial clocks (e.g. Verbiest et al. 2009) and thus excellent tools in the ongoing endeavours of high-precision gravity tests (Kramer et al. 2006), neutron-star equations of state (Demorest et al. 2010; Özel et al. 2010) and gravitational wave detection (van Haasteren et al. 2011; Yardley et al. 2011; Demorest et al. 2013; Shannon et al. 2013). These experiments utilize the high-precision timing of millisecond pulsars (MSPs), which are known for their rotational stability and the stability of their integrated pulse profiles (which do not change over many years). However, recent studies have shown that the profiles of MSPs can exhibit low-level instabilities that may limit the achievable timing precision. In general, these instabilities can be categorized into two types: temporally uncorrelated variabilities caused by the instability of single pulses (e.g. Jenet et al. 1998;

Liu et al. 2012; Shannon & Cordes 2012) and temporally correlated variations induced by other phenomena (e.g. Kramer et al. 1999; Edwards & Stappers 2003). The contribution of jitter to the pulsar timing noise could be mitigated by simply increasing the exposure time or by correcting the biased integrated profiles with suitable algorithms (Cordes & Shannon 2010; Osłowski et al. 2013). Comprehensive studies of profile instabilities would give new insights into the fundamental timing limits and thereby potentially improve the timing precision, which is essential for the aforementioned astrophysical experiments.

PSR J1022+1001 is a MSP with a rotation period of approximately 16 ms. It exhibits a regular rotational behaviour and is included in the current pulsar timing array observations for the purpose of gravitational wave detection (e.g. Manchester 2013). The pulsar is in a binary with a 7.8-d orbital period with a white dwarf companion and is thus a potential laboratory for testing the strong equivalence principle (e.g. Freire et al. 2012; Antoniadis et al. 2013). The integrated pulse profile of the pulsar consists of a double-peaked structure at *L*-band frequencies with a highly

★ E-mail: kliu.psr@googlemail.com

linearly polarized trailing component. The amplitude ratio of the two components has been shown to change significantly as a function of frequency (Ramachandran & Kramer 2003). There is also evidence that the ratio is unstable across time and may even evolve on short time-scales of tens of minutes (Kramer et al. 1999; Purver 2010). Meanwhile, as the trailing component of the pulse profile is highly polarized, profile instability could also arise from improper polarization calibration due to an imperfect receiver model (Hotan, Bailes & Ord 2004a). A better understanding of the profile variation in this system is therefore essential, in order to improve the timing precision of PSR J1022+1001 further. This may be used to assess and perhaps correct for profile variations in other MSPs.

Examining single pulses has not been common in MSPs, owing to their typically lower flux densities compared with normal pulsars. Exceptions are the so-called giant pulses, which have been detected only in a few bright MSPs (e.g. Cognard et al. 1996; Romani & Johnston 2001; Joshi et al. 2004; Knight et al. 2005). Analysis of weak single pulses has only been carried out in the few brightest MSPs (Jenet et al. 1998; Jenet, Anderson & Prince 2001; Edwards & Stappers 2003; Shannon & Cordes 2012; Osłowski et al. 2014). Based on an autocorrelation analysis, Edwards & Stappers (2003) have shown evidence for pulse intensity modulation at the phase of the trailing component in PSR J1022+1001. However, no detailed investigation into single pulses has been undertaken so far, due to either limited system sensitivity or the lack of high-resolution instrumentation.

The rest of this article is structured as follows: In Section 2 we describe the details of the observations and data processing. Results for the single pulses detected, integrated profile stability and timing analysis are presented in Section 3. We conclude and discuss the results in Section 4.

2 OBSERVATIONS

Simultaneous observations of PSR J1022+1001 of 7–9 h duration were conducted with the Westerbork Synthesis Radio Telescope (WSRT) and the Effelsberg 100-m Radio Telescope, at four epochs. A summary of these observations can be found in Table 1. The two telescopes were chosen as they provide similar sensitivities in the *L* band, so that profile instability could be verified from both sites at the same time. In addition, Effelsberg is an alt–azimuth telescope,

Table 1. Parameters of simultaneous observations of PSR J1022+1001 with the WSRT and the Effelsberg 100-m Radio Telescope. The symbols T, f_o and Δt_s represent the duration of the observation, overlapping observing frequency range and single-pulse time resolution at the WSRT.

MJD	T (hr)	f_o (MHz)	Δt_s (μs)
55909	7.0	1300–1440	4.0
55974*	8.4	1300–1440	4.0
56158	8.5	1300–1440	2.0
56257	9.0	1300–1365†	2.0

Notes.
*At this epoch, the Effelsberg data were corrupted due to a problem with the signal attenuators (see Appendix A for more details).
†At this epoch, three 25-MHz sub-bands of Effelsberg data were lost due to hard drive failure.
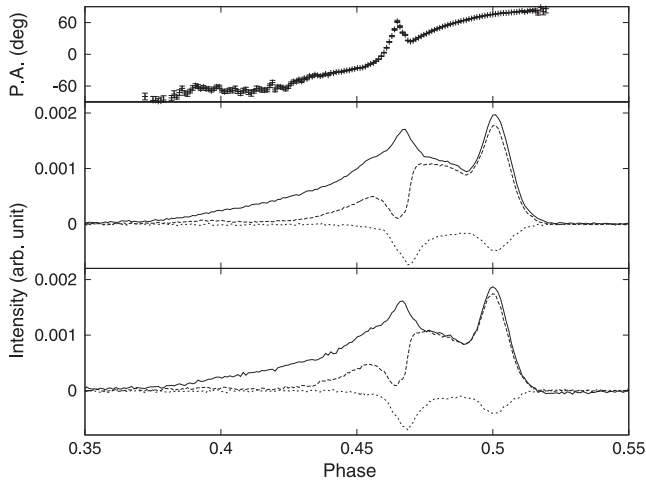
meaning that it tracks a source across the sky; the changing parallactic angle (PA) results in varied Stokes parameters, which need to be properly calibrated. On the other hand, the WSRT is equatorially mounted with no PA variation and thus in principle is not influenced by this effect. Therefore, using data from these two telescopes allows us to cross-check the results of polarization calibration, which was claimed to be the main cause of profile instability (Hotan et al. 2004a; van Straten 2013).

At the WSRT, we used the PuMa-II system to record eight-bit baseband data (Karuppusamy, Stappers & van Straten 2008), which were later processed offline in two stages. In the first stages, the 8 × 20 MHz bands were combined to form a multiband data stream corresponding to a 160-MHz contiguous band centred at 1380 MHz, at the original time resolution of 25 ns. The DSPSR software (for details see van Straten & Bailes 2011) was used to dedisperse the data coherently over the entire bandwidth using a 64-channel synthetic software filter bank at the dispersion measure of 10.246 cm^{-3} pc and folded to form 10-s averages in the second stage. Additionally, we searched for significant single pulses at this stage. This was done after summing up the total intensities of all frequencies and averaging by the number of frequency channels. Any pulse period that contained a peak greater than five times the root-mean-square error (rms) of the off-pulse noise was written out as a single-pulse candidate. In the post-processing stage, these were then confirmed to be true pulses by comparing the phase with that of the integrated pulse profile.

At Effelsberg, the new PSRIX pulsar backend (Karuppusamy et al., in preparation) was used in baseband mode. These data were reduced in the same way as the WSRT data, except that, here, 8 × 25 MHz bands were produced with a central frequency of 1347.5 MHz. In addition, at regular intervals of 40 min, the telescope was pointed 0°.5 off-source for 90 s, when a pulsed noise signal was injected at 45° into the feed probes as a calibrator for polarimetry.

The 10-s integrations and single pulses were then processed with the PSRCHIVE software package (Hotan, van Straten & Manchester 2004b). For the 10-s integrations from Effelsberg, we performed polarization calibration with the single-axis receiver model, which corrects for the differential gains between the two feeds.[1] Next we used PSRCHIVE'S INTERACTIVE RFI ZAPPER (PAZI) to clean the radio-frequency interference (RFI) by visual examination of the averaged pulse profiles and single-pulse candidates. Finally, we selected all 10-s integrations that overlapped in time between the two telescopes and then removed the non-overlapping frequency channels, leading to an overlapping observing frequency range of 1300–1440 MHz.

Example polarization profiles of PSR J1022+1001 from both the WSRT and the Effelsberg observation at MJD 56257 centred at 1320 MHz can be found in Fig. 1. The integrated profile shows a double-peaked structure, with the trailing component consisting of highly linearly polarized emission. The polarization properties are in agreement between the two sites, with a correlation coefficient of 0.999 (as defined in Liu et al. 2012). Given the profile instability of this pulsar, especially in observations separated by several years (Purver 2010), the polarization components agree qualitatively with previous observations (Kramer et al. 1999; Ramachandran & Kramer 2003; van Straten 2013).

---

[1] http://psrchive.sourceforge.net/manuals/pac/

Figure 1. Polarization profiles of PSR J1022+1001 obtained at MJD 56257 from the Effelsberg (middle) and the WSRT (bottom) observation at 1.3 GHz. P.A. in the top panel stands for the polarization position angle of the linear component. The Effelsberg and WSRT data show consistent P.A. curves and here we plot the one from the Effelsberg data as a demonstration. The solid, dashed and dotted lines represent the Stokes parameters I, L and V, respectively. There is a 'negative' dip, i.e. an underestimation of system temperature, in the WSRT total intensity profile (at phase 0.52), which corresponds to the low-bit sampling artefact discussed in Jenet & Anderson (1998). This is due to the fact that the signal was originally quantized using 2 bits per sample at each individual dish of the WSRT. Further investigation shows that the dip is mostly from high-frequency channels within each 20 MHz band. The total intensity profile is slightly lowered by this underestimation, which makes the valley region between the two components appear overpolarized. Further investigations can be found in Appendix A.

3 RESULTS

3.1 Subpulse properties

In a total of 35 h of observations, we have approximately 14 400 single-pulse detections above our 5σ threshold, which corresponds to about 700 subpulses[2] located in the leading component of the integrated profile and about 13 700 in the trailing component.[3] The detections were all made from the observations at MJD 55909 and 56257, as the pulsar was significantly weaker due to interstellar scintillation at MJD 55974 and 56158. The highest peak signal-to-noise ratio of detection is close to 10. Fig. 2 shows the subpulse detections achieved at MJD 56257 at their occurrence epochs and peak signal-to-noise ratios (S/N_s) relative to the local average S/N of all single pulses observed during the 5-min interval centred at the epoch of the single pulse ($\langle S/N_s\rangle_{5min}$). We can see that there is an evolution in the ratio, which is due to the pulsar flux decreasing because of interstellar scintillation. With our sensitivity, useful detections are feasible only when integrating 5-min observations results in a profile of peak S/N (S/N_{5min}) above 30. The detection rate is highest between MJD 56257.055 and 56257.060, corresponding to 4.5 per cent of all rotations. We have calculated time separations between neighbouring subpulses in the trailing component within

[2] In each rotation, the pulsar produces a single pulse, which can be composed of one or more subpulses. This reflects our situation better, as occasionally more than one subpulse can be detected from a single period.

[3] The leading- and trailing-component pulses are distinguished by an arbitrary bound of rotational phase 0.485 in Fig. 1.
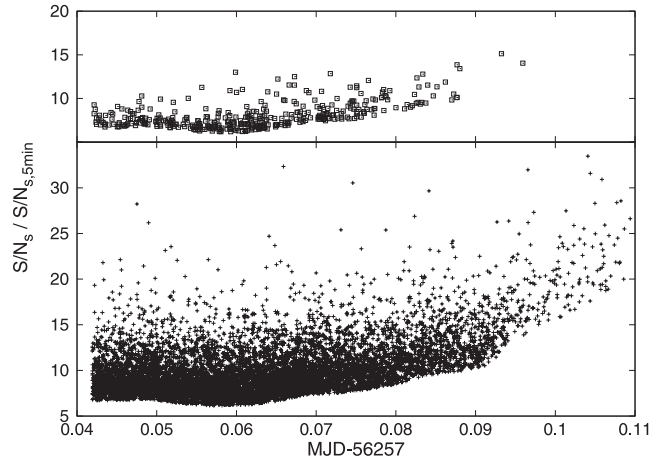
Figure 2. subpulses detected at MJD 56257 as a function of time and their peak signal-to-noise ratios (S/N_s) divided by the local average S/N of all single pulses observed during the 5-min interval centred on the epoch of the single pulse ($\langle S/N_s\rangle_{5min}$). The location of the peak bin was selected based on a 16-μs time resolution. The top panel shows detections at the phase of the leading component in the averaged profile and the bottom panel shows detections at the phase of the trailing component.
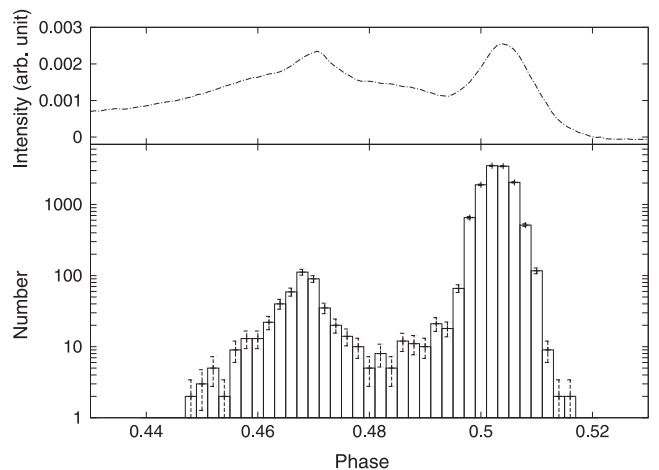

Figure 3. Distribution of peak amplitude phase for all detected subpulses (lower panel), in comparison with the integrated profile (upper panel). Again, the peak bins were chosen based on a 16-μs time resolution. The integrated profile is from the WSRT observation at MJD 56257.

this period of time and over 95 per cent of them are smaller than 1 s, indicating that pulse nulling with duration longer than 1 s ($\simeq$60 rotations) is not detected.

Fig. 3 shows the distribution of the peak amplitude phases for the detected subpulses, compared with the integrated profile. All detections were obtained within the on-pulse phase and most of them are clustered within the range defined by the trailing component in the average profile. The two maxima correspond to the two peaks in the phase-resolved modulation index of Edwards & Stappers (2003). In Fig. 4, we plot the distribution of the flux densities of the subpulses divided by the averaged flux densities of a single pulse in 5-min integrations. The plot demonstrates that none of the detections has a flux density that is above 3.8 times the average and there is therefore no evidence for giant pulses.

Fig. 5 presents example polarization profiles of subpulses at the phases of the leading and trailing components. It can be seen that pulses from the leading component do not show significant
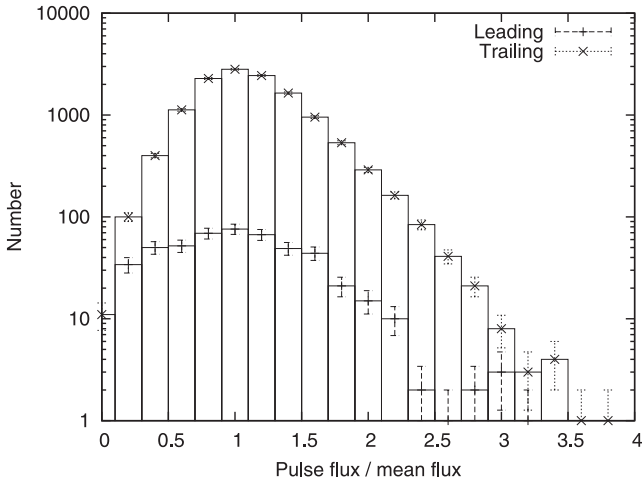
Figure 4. Distributions of flux densities relative to averaged single-pulse flux densities in 5-min integrations, for subpulses detected in the leading and trailing components, respectively. No pulse with a flux above 3.8 times the average has been seen.

polarization, while those from the trailing component are highly linearly polarized. The polarization fractions of both components are consistent with the integrated pulse profile, suggesting that the detected subpulses represent the bright end of the energy distribution of all pulses. The bottom plot in Fig. 5 shows the averages of the leading- and trailing-component pulses,[4] respectively, the polarization characteristics of which are in agreement with the corresponding individual detections. It is interesting to note that in both averages, the components that do not include detected subpulses are consistent with the average of all periods in total intensity. This means that during the occurrence of bright emission in one component, there still exists emission at an average level at the location of the other component.

Meanwhile, subpulses can be detected from the leading and trailing components within the same pulse period. In total, about 280 such events have been detected. In all events, the two phases of peak amplitude are well separated from the phase bound 0.485 (used to group the detections), excluding detections of a single pulse with broad width spreading over the region of both components. We will later refer to such an event as a 'bi-pulse' and the corresponding integrated profile is shown in Fig. 6. The valley region between the two components is significantly steeper in this profile than the ordinary average in Fig. 1, while the polarization properties of the two components are consistent. To investigate the correlation of occurrence between the leading- and trailing-component pulses, we carried out a further statistical study. Pulses were selected at both epochs, from the period of time when the leading-component pulses could be detected. A summary of the selections can be found in Table 2. We formed the statistical test problem in the following statement:

$$\begin{cases} H_0 : \text{Leading and trailing pulses are uncorrelated.} \\ H_1 : \text{Leading and trailing pulses are correlated.} \end{cases}$$

The bi-pulse phenomenon is defined as a case in which both the leading- and trailing-component pulses are detected within a single

---

[4] Here we selected pulses with 5σ detection in only one component. Occasionally, bright emission can occur in both components within a single period, which will be discussed in the next paragraph.
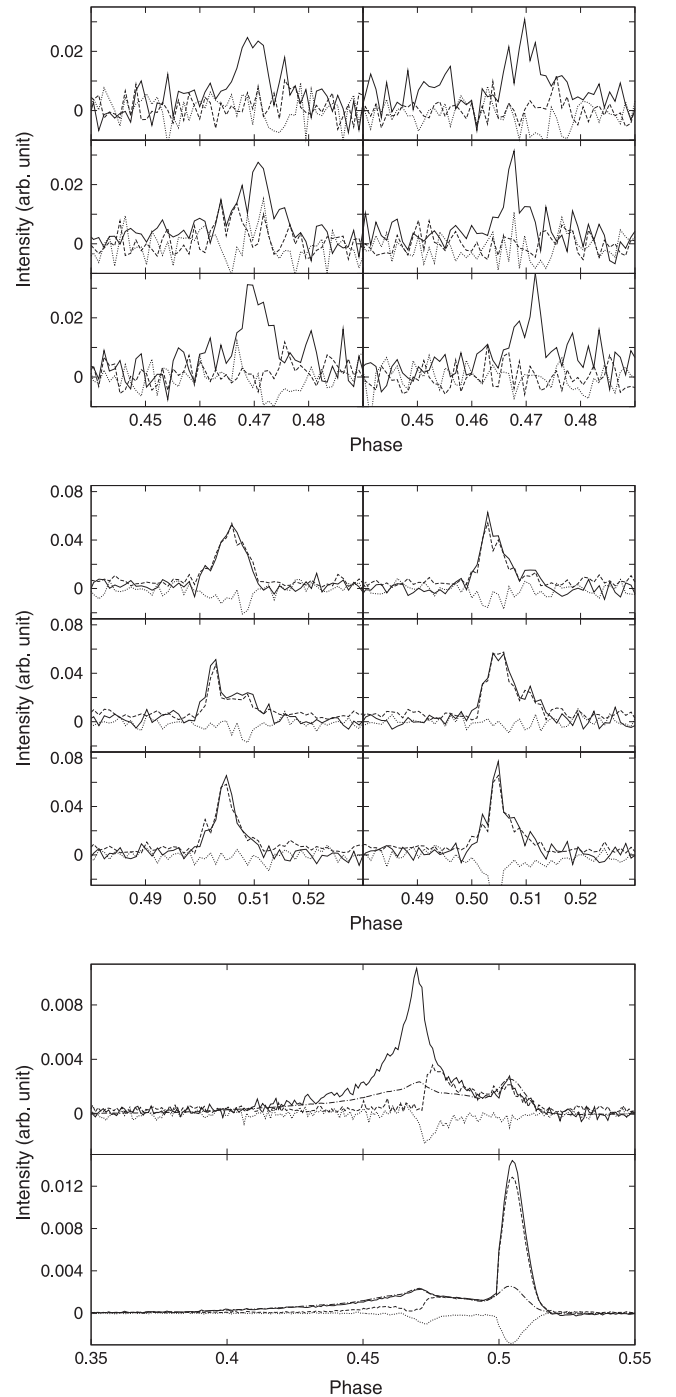

Figure 5. Example polarization profiles of subpulses detected at MJD 56257, at the phase of the leading (top) and trailing (middle) components in the average profile. The bottom plot shows the integrations of detected subpulses from the leading (upper panel) and trailing (lower panel) components, respectively. The solid, dashed and dotted lines stand for Stokes *I*, *L* and *V*, respectively. The dot–dashed line represents the averaged total intensity of all periods.

period. Thus, under the null hypothesis H_0, in each pulse period the probability of observing bi-pulses is

$$P_b = P_l P_t, \tag{1}$$

where P_b, P_l and P_t are the probabilities of observing bi-, leading- and trailing-component pulses, respectively. By combining the
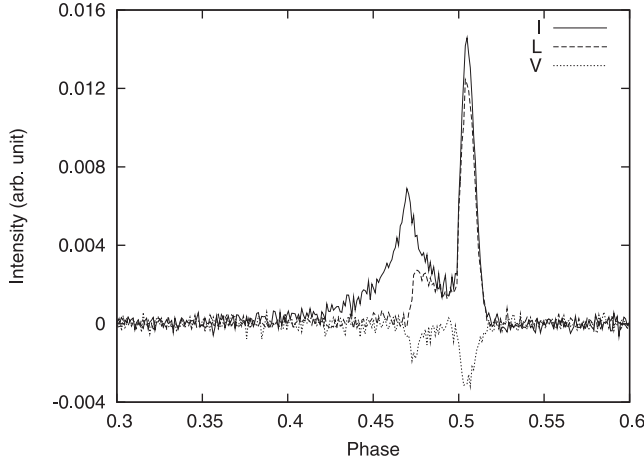
Figure 6. Polarization profile averaged over all detected bi-pulses, where subpulses were detected in both components within a single period.

Figure 7. Distribution of pulses from the trailing component by their relative S/N_s and width. To avoid bias caused by the time-variant detection threshold, only pulses with epoch between MJD 56257.042 and 56257.066 and $(S/N_p)/(\langle S/N_s \rangle_{5min}) > 7$ were selected. Again, the peak bins were selected based on a 16-μs time resolution.

Table 2. Summary of selected pulses used to investigate the occurrence correlation between the leading- and trailing-component pulses. Here N, N_l, N_t and N_b denote the number of periods within the time range the pulses were chosen from, number of leading- and trailing-component pulses and number of bi-pulses, respectively. The probability of detecting more than N_b bi-pulses is denoted by $P(n \geq N_b)$

Phase	MJD 55909	MJD 56257
N	2.1×10^5	2.0×10^5
N_l	72	525
N_t	2737	7929
N_b	25	234
$P(n >= N_b)^\star$	10^{-252}	10^{-881}

Note. *Due to difficulties in numerical evaluation of the integral, we used asymptotic values for the error function. This could result in an error of one order of magnitude, but will not change the conclusion.

statistics from these two epochs, we have calculated the observed P_l and P_t, which gives an expected value of P_b of $3.80 \pm 0.16 \times 10^{-5}$ under the null hypothesis H_0. Meanwhile, the observed bi-pulse occurrence probability was calculated to be $6.32 \pm 0.39 \times 10^{-4}$, about 17 times larger. For a more quantitative study, over N pulse periods the statistical distribution functions f of the total number of bi-pulses, leading- and trailing-component pulses are

$$f(N_b|P_b, N) = C_N^{N_b} P_b^{N_b}(1 - P_b)^{N-N_b}, \qquad (2)$$

$$f(N_l|P_l, N) = C_N^{N_l} P_l^{N_l}(1 - P_l)^{N-N_l}, \qquad (3)$$

$$f(N_t|P_t, N) = C_N^{N_t} P_t^{N_t}(1 - P_t)^{N-N_t}, \qquad (4)$$

where C_b^a is the binomial coefficient, defined as $C_b^a = (b!)/(a!(b-a)!)$. Using the Bayesian theorem with a flat prior for the distributions of probability of each type of pulse, we have

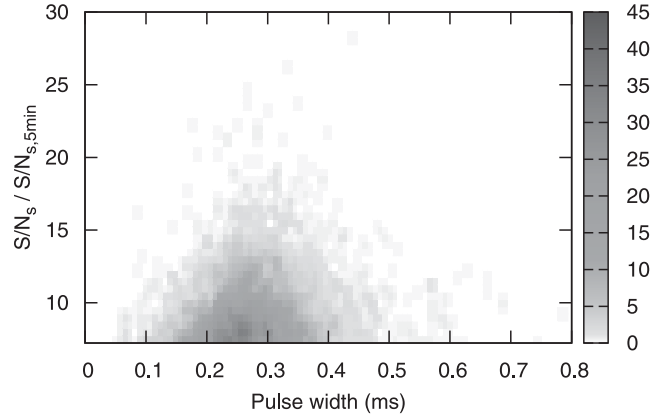$$f(P_l|N_l, N) = f(N_l|P_l, N)(N + 1), \qquad (5)$$

$$f(P_t|N_t, N) = f(N_t|P_t, N)(N + 1), \qquad (6)$$

where $f(P_l|N_l, N)$ and $f(P_t|N_t, N)$ are the posteriors for P_l and P_t. Thus the probability distribution of N_b given N_l and N_t is

$$\begin{aligned} f(N_b|N_l, N_t, N) = \int_0^1 \int_0^1 dP_l\, dP_t\, C_N^{N_b}(P_l P_t)^{N_b} \\ \times (1 - P_l P_t)^{N-N_b} \\ \times f(P_l|N_l, N)f(P_t|N_t, N). \end{aligned} \qquad (7)$$

Under the null hypothesis H_0, we have

$$P(N_b > N_B \text{ or } N_b < N_A) = 1 - \sum_{N_A}^{N_B} f(N_b|N_l, N_t, N), \qquad (8)$$

where $P(N_b > N_B \text{ or } N_b < N_A)$ is the probability of finding that the occurrence of bi-pulses N_b is greater than the threshold N_B or less than the threshold N_A, under the assumption that the leading- and trailing-component pulses are uncorrelated. This provides a good statistic for testing whether the observations agree with the null hypothesis H_0. Accordingly, we have estimated the probability of detecting more than N_b bi-pulses ($P(n >= N_b)$) based on the statistics in Table 2, which appears to be very close to zero at both epochs. We therefore conclude that the leading- and trailing-component pulses are correlated in their occurrence, otherwise it would be extremely rare to observe such a high value of N_b with the null hypothesis H_0. In young pulsars, correlated emission modulation at different rotational phases has been found in a few cases (Weltevrede, Wright & Johnston 2012; Karuppusamy et al., in preparation).

Jenet et al. (1998) showed an inverse correlation between pulse width and peak amplitude for the subpulses of PSR J0437−4715. In Fig. 7, we perform the same investigation by showing the distribution of detected pulses from the trailing component on a width–relative S/N_s plane. Here, to avoid bias caused by a variable detection threshold, we only selected detections between MJD 56257.042 and 56257.066 and with $(S/N_s)/(\langle S/N_s \rangle_{5min}) > 7$. It is interesting to note that, instead of an anticorrelation, there exists a favoured pulse width[5] value of about 0.25 ms, which is consistent for pulses of different relative S/N_s values. Also, the probability of occurrence does

---

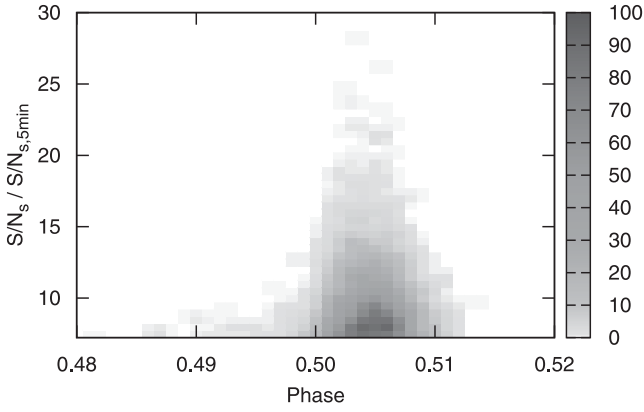[5] Here the pulse width is defined by the on-pulse region.

Figure 8. Distribution of the same pulses as in Fig. 7 on a phase−relative S/N_s plane.

not favour pulses with narrow width and high peak amplitude. Fig. 8 gives the distribution of the same pulses with respect to their phases and relative S/N_s. The plot demonstrates that the occurrence phases of the subpulses are strongly clustered, especially for those with a peak 10 times above average. The phenomenon that brighter pulses show up earlier in phase, found for PSR J1713+0747 in Shannon & Cordes (2012), is not seen. The property of regular shape and phase could possibly be translated into precise pulse time-of-arrival (TOA) measurements, which will be investigated further in Section 3.3.

3.2 Variation of integrated profiles and subpulse occurrence

As mentioned in Section 1, it has not been shown conclusively whether the average profiles of PSR J1022+1001 exhibit intrinsic shape variation. Here, following the idea of previous analyses (e.g. Kramer et al. 1999), we calculate the amplitude ratio of the leading and trailing components of total intensity profiles for 10-min integrations and plot them against time. For each component, the amplitudes were defined as the total intensity within a fixed phase range (1.7 per cent of a period), after subtracting the baseline. Their errors were calculated from the rms of the off-pulse bins. We used a 40-MHz sub-band ranging from 1300–1340 MHz, where, for most of our observing time, the flux density is the highest within the entire overlapping band. The results from data at MJD 55909 and 56257 are shown in Fig. 9, where at both epochs the measurements show a clear evolution with time and are consistent between the two sites. The variation trend is similar to that indicated in fig. 3.6 of Purver (2010). We also calculated the weighted correlation coefficient (ρ_w) between trends from the two sites, which is defined as

$$\rho_w = \frac{\text{cov}_w(\mathcal{E}_i, \mathcal{W}_i, \sigma_{\mathcal{E},i}, \sigma_{\mathcal{W},i})}{\sqrt{\text{cov}_w(\mathcal{E}_i, \mathcal{E}_i, \sigma_{\mathcal{E},i}, \sigma_{\mathcal{E},i})\text{cov}_w(\mathcal{W}_i, \mathcal{W}_i, \sigma_{\mathcal{W},i}, \sigma_{\mathcal{W},i})}}. \quad (9)$$

Here $\mathcal{E}_i$, $\mathcal{W}_i$ are the ratio measurements from Effelsberg and WSRT, respectively, $\sigma_{\mathcal{E},i}$, $\sigma_{\mathcal{W},i}$ are their measurement errors and cov_w is the weighted covariance, defined by

$$\text{cov}_w(x_i, y_i, \sigma_{x,i}, \sigma_{y,i}) = \frac{\sum_i (x_i - \overline{x})(y_i - \overline{y})/(\sigma_{x,i}^2 \sigma_{y,i}^2)}{\sum_i 1/(\sigma_{x,i}^2 \sigma_{y,i}^2)}, \quad (10)$$

where the overline stands for the weighted mean. The calculated ρ_w is 0.60 at MJD 55909 and 0.91 at MJD 56257, respectively, confirming that measurements from the two sites exhibit the same evolution trend. Note that, at the beginning of MJD 56257, the pul-
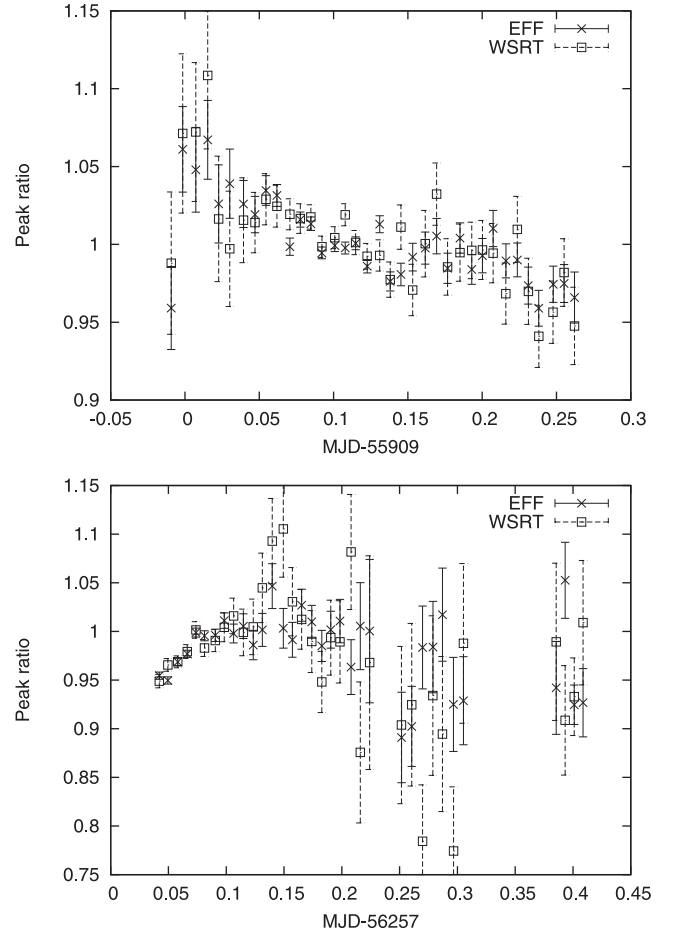

Figure 9. Amplitude-ratio measurements of the two components in the PSR J1022+1001 total intensity profiles from two epochs. The measurements were made using 10-min integrations of a 40-MHz band centred at 1320 MHz. Note that measurements of fractional error larger than 10 per cent were discarded, which leads to the gap within the results at MJD 56257.

sar was significantly brighter and the profile was showing a steeper variation trend than at MJD 55909, which thus corresponds to a value of ρ_w closer to unity. To understand the estimation error of ρ_w, we performed a Monte Carlo simulation. In each iteration, we randomly altered the measured component amplitudes based on Gaussian distributions with standard deviation equal to the measurement errors and thus calculated a new amplitude ratio and ρ_w. Fig. 10 shows the histogram of ρ_w with 10 000 iterations obtained from measurements at MJD 56257, where ρ_w is larger than 0.78 and 0.64, with 68 per cent and 95 per cent confidence level, respectively. The same investigation has also been performed for the measurements at MJD 55909 and the corresponding thresholds are 0.40 and 0.20, respectively. These likely rule out the possibility of a non-correlation between the two sites. A brief summary of the results can be found in Table 3.

To investigate the effect of polarization calibration on our results, we also applied the template-matching calibration technique to the Effelsberg data at MJD 55909 and 56257 (van Straten 2006; Lee et al., in preparation), based on the template polarization profile from the European Pulsar Network Pulse Profile Database (Stairs, Thorsett & Camilo 1999), showing consistent polarimetry with previous published results. For this calibration scheme, we used both the single-axis and the reception description of the receiver
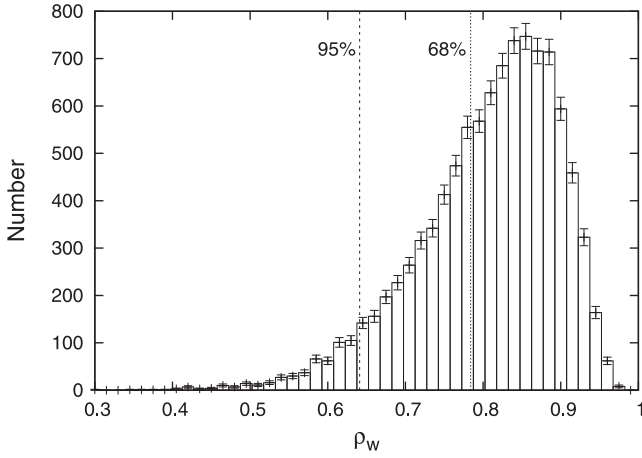
Figure 10. Distribution of 10^4 simulated values of ρ_w based on amplitude-ratio measurements from data obtained at MJD 56257.

Table 3. Weighted correlation coefficient (ρ_w) between the amplitude-ratio measurements from the WSRT and Effelsberg data at two epochs, as well as their lower limits, with 68 per cent ($\mathcal{L}_{68}$) and 95 per cent ($\mathcal{L}_{95}$) confidence levels.

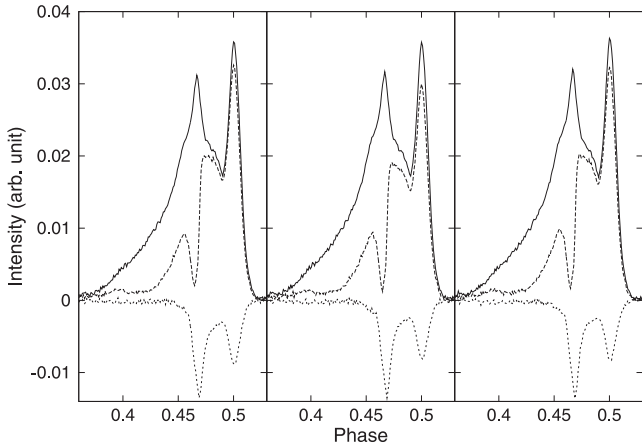| MJD	ρ_w	$\mathcal{L}_{68}$	$\mathcal{L}_{95}$
55909	0.60	0.40	0.20
56257	0.91	0.78	0.64

Figure 11. Comparison of Effelsberg polarization profiles obtained from data at MJD 56257, based on a calibrator+single-axis model (left), template+reception model (middle) and template+single-axis model (right). The solid, dashed and dotted lines stand for Stokes parameter I, L and V, respectively.

properties, the latter of which models both the differential gain and the cross-coupling of the two feeds (Ord et al. 2004; van Straten 2004). The calibrated data were then processed by following the same procedure as described above. Both receiver models led to a fit with reduced χ^2 close to unity. Still, the effect of feed cross-coupling was estimated to influence the total intensity profile by less than 1 per cent and the true value could not be measured, due to limited sensitivity. As a demonstration, in Fig. 11 we show the polarization profiles obtained from MJD 56257 data with the cali-
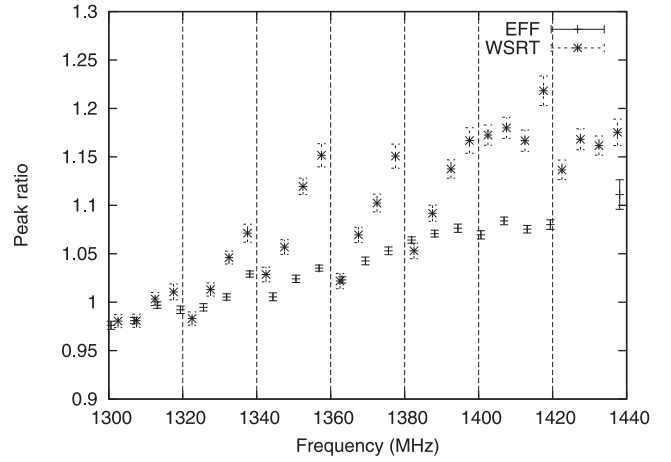

Figure 12. Measured amplitude ratios as a function of frequency, from the profile models obtained at MJD 55909. The measurements from the Effelsberg and WSRT data are based on profiles of bandwidth 6.25 and 5 MHz, respectively. The edges of the 20-MHz sub-bands (starting from 1300 MHz) in the WSRT data have been marked by dashed lines. Note that for the WSRT data there is an additional increase of the measurement values within a sub-band, associated with the low-bit digitization artefact shown in Fig. 1. More details of this effect are shown in Appendix A.

bration result based on calibrators and the single-axis model shown in Fig. 1. It can be seen that the three profiles from different calibration schemes or models exhibit consistent polarization properties, especially the two achieved with the single-axis model. Using the reception model results in a slightly lower linear polarization percentage (middle panel), mostly due to absorption of power into the feed leakage terms. In addition, the calculated ρ_w between the new amplitude-ratio measurement trend and the WSRT result is 0.89 when using the reception model and 0.91 when single-axis calibration was applied. These are almost the same as the value obtained above. The same analysis for MJD 55909 data led to $\rho_w = 0.55$ when using the reception model and $\rho_w = 0.60$ when applying single-axis calibration, also consistent with the result based on calibrators. Further investigation based on independent Effelsberg data for the Large European Array for Pulsars project (Kramer & Stappers 2010) shows that the circular receiver does not suffer from strong cross-coupling between the two feeds (Lee et al., in preparation), which validates the use of the single-axis model in this case. Therefore, it is highly unlikely that our detected profile variation is due in large part to improper polarization calibration.

Note that the profile shape has a clear frequency dependence (e.g. Ramachandran & Kramer 2003). If the flux density distribution within the observing band changes significantly in time due to interstellar medium diffractive scintillation, the averaged profiles (after frequency summation) may therefore also exhibit time-variant behaviour (e.g. Liu et al. 2011). To understand its contribution to our results, here we simulate the varying trends produced by this effect and compare them with the real measurements. At each epoch, we first used an integrated profile for the entire duration of the observation to establish a profile model with frequency-dependent shape. As an example, Fig. 12 shows the measured amplitude ratios as a function of frequency[6] from the profile models for the MJD 55909

---

[6] The phase ranges defined to calculate component amplitudes are identical for all central frequencies, as the data were already de-dispersed, as mentioned in Section 2.
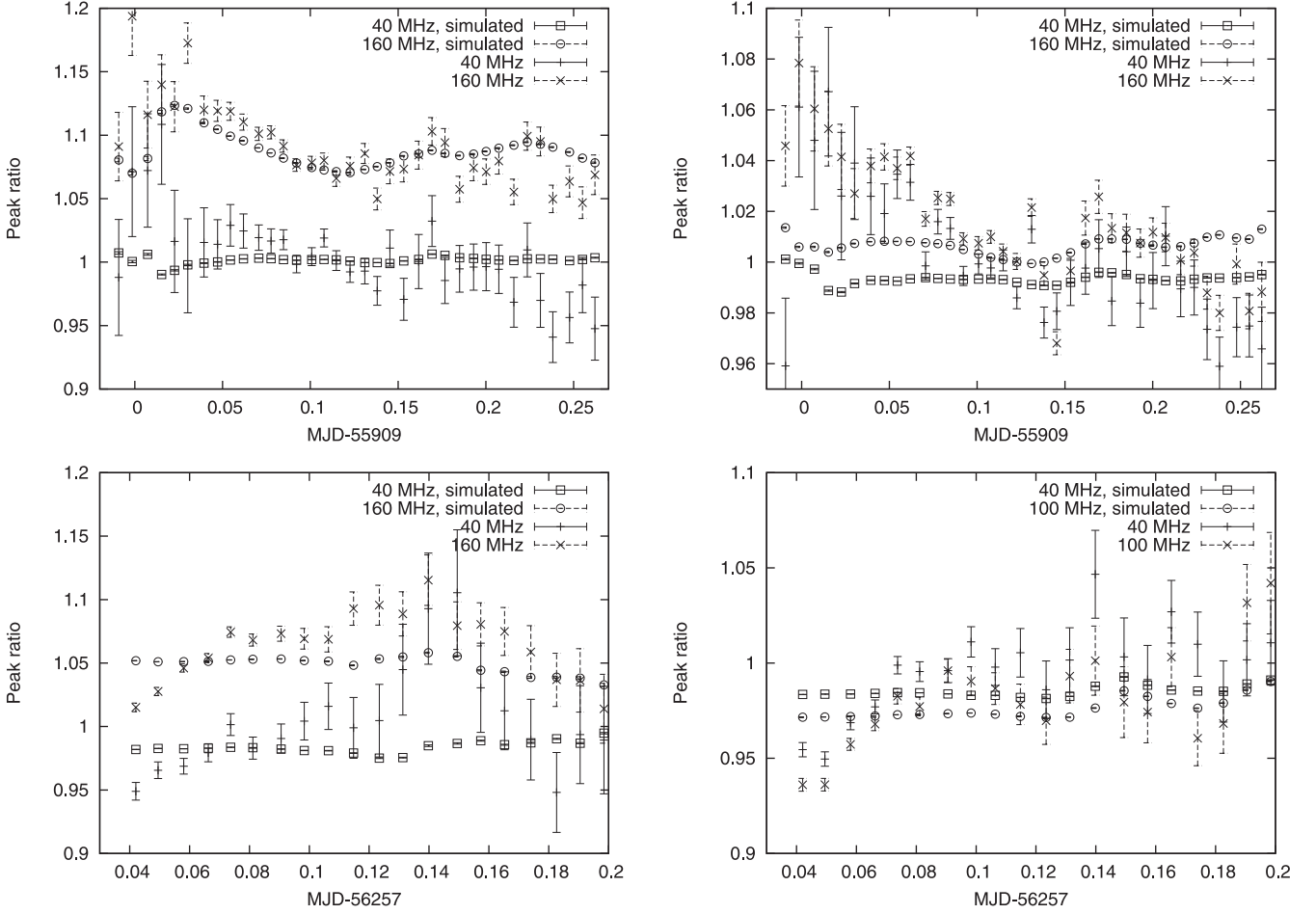
Figure 13. Simulated peak amplitude ratios based on flux densities measured from 10-min integrations, compared with the actual ratio measurements. The simulations were carried out on both WSRT (left) and Effelsberg (right) data at MJD 55909 (top) and 56257 (bottom), using both the 40-MHz sub-band and the entire available bandwidth. The uncertainties of the simulated ratios are typically of order $\lesssim 10^{-3}$ and thus are not visible from the plots. Note that for MJD 56257 the analysis was carried out only for the first half of the data, as in the second half the flux densities within individual frequency channels were not measurable on many occasions, due to low S/N. The effective observing bandwidth of Effelsberg at MJD 55909 is 160 MHz, due to a receiver cut-off below 1280 MHz.

data. We then applied the measured frequency-dependent flux densities from each 10-min integration to the model to create a simulated profile and computed the resulting amplitude ratio after frequency summation. For this purpose, we kept the frequency resolution of 6.25 MHz for the Effelsberg data and 10 MHz for the WSRT data, so as to have enough signal within each frequency channel. The channel width is significantly smaller than the estimated scintillation bandwidth of this pulsar (Cordes & Lazio 2002; You et al. 2007). The uncertainties in the amplitude ratios of the simulated profiles were calculated from the measurement errors of the flux densities estimated from each frequency channel of each 10-min integration. The flux densities, as well as their errors, were measured using PDV (psrchive's archive data displayer), where the flux density is defined as the total intensity within a pulse period after subtracting the baseline; their errors were calculated from the rms of off-pulse phase bins defined by the 3σ threshold. By following this procedure, the observed variation trend would be reproduced if the profile instability were mostly dominated by the scintillation effect. In Fig. 13, we present the results at MJD 55909 and 56257 from both sites, based on both the selected 40-MHz sub-band and the entire bandwidth. Clearly, in most cases the simulation resulted in a flat

trend and did not reproduce the actual measurements.[7] The reduced χ^2 of the measurement series with respect to the corresponding simulated trend[8] fell between 2.0 and 22, significantly above unity. We therefore conclude that our detected profile instability shown in Fig. 9 is not significantly affected by the scintillation effect.

We do not detect profile variation at the other two epochs, MJD 55974 and 56158, mostly because the source was comparatively dim due to scintillation. At these two epochs, with the WSRT 160-MHz observations the $S/N_{5\mathrm{min}}$ values are all below 30, while the

---

[7] Note that an exceptional case may be drawn from the simulation over full bandwidth of the WSRT data from MJD 55909. This indicates that profile evolution based on the large bandwidth could have a significant contribution from the scintillation effect. The reason why the simulation based on Effelsberg data from the same epoch did not reproduce the variation trend is that our Effelsberg profile shows significantly less frequency dependence and is thus less affected by the scintillation effect.

[8] Defined as $\frac{1}{N_{\mathrm{r}}-1}\sum_i \frac{(r_i - s_i)^2}{\sigma_{r,i}^2 + \sigma_{s,i}^2}$, where N_{r} is the number of amplitude ratios, r_i, s_i are amplitude ratios from the real measurement and simulation, respectively, and $\sigma_{r,i}$, $\sigma_{s,i}$ are their errors.
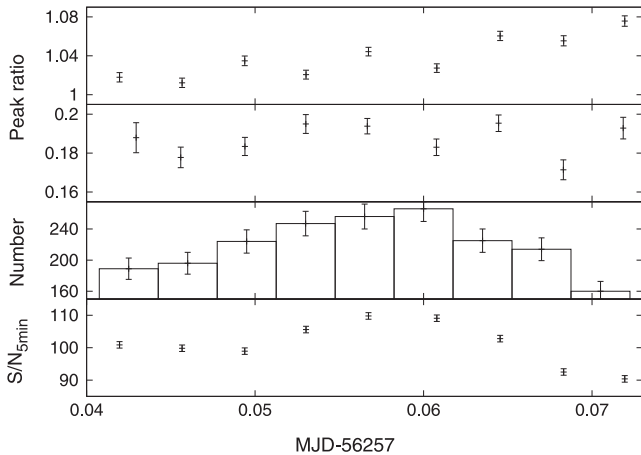
Figure 14. Top to bottom: amplitude-ratio measurements from 5-min integrations and from subpulse averages, numbers of subpulses in 5 min and S/N of 5-min integrations. Here the subpulses were selected with $(S/N_s)/(\langle S/N_s \rangle_{5\text{min}}) > 9$ and MJD between 56257.042 and 56257.074. The 5-min integrations were formed from WSRT data.

maxima at MJD 55909 and 56257 reach 75 and 110, respectively. This may explain the contradictory conclusions from previous studies on profile stability on short time-scales. In addition, it can be seen from Fig. 9 that the amplitude-ratio variation may not be significant enough for detection within 0.1 d, which is the longest observation used in previous work. Therefore, detection of profile instability is achievable only when the pulsar is bright and the variation is large.

We note that our analysis draws seemingly different conclusions on the profile stability of PSR J1022+1001 compared with Liu et al. (2012), for a few reasons. First, our new observations detected the pulsar when it was significantly brighter than in previous cases. For instance, at the beginning of the MJD 56257 observation, an integration time of 1800 s led to a profile with S/N of over 800, while integrating the entire observation (approximately 1900 s) in Liu et al. (2012) only resulted in a value of about 480. Secondly, the work in Liu et al. (2012) was based on 1-min integrations and thus focused more on searching for random variations in profile shapes on short time-scales. Finally, the duration of the previous observation does not provide sensitivity to profile variations on a time-scale of several tens of minutes as detected in this article.

In principle, the profile variation can be fully attributed to the detected bright subpulses if either their shape or occurrence rate varies by a sufficiently large amount in time. Such a possibility has been investigated in Fig. 14. To balance between the potential shape bias introduced by a variable detection threshold and the time span allowing us to see profile variation, here we selected subpulses detected with $(S/N_s)/(\langle S/N_s \rangle_{5\text{min}}) > 9$ and MJD between 56257.042 and 56257.074. It can be seen that, while the amplitude ratio from 5-min integrations gradually increases in time (≈ 6 per cent from MJD 56257.04 to 56257.07), no similar variation trend is witnessed from the averages of the subpulses. This indicates that the profile variation is not caused by the selected bright subpulses. In fact, the number of detected subpulses is approximately 200–300 per 5-min window (1–1.5 per cent of all periods). Therefore, the amplitude ratios of the subpulse averages would need to change by a factor of 4 or more if variability in the 1–1.5 per cent of subpulses detected were the cause of the profile variation in 5-min integrations. Note that the number of detected subpulses remains consistent in time, though it is proportional to the S/N of 5-min integrations, which is expected due to variability in detection sensitivity. This suggests

that the profile variation is not induced by the occurrence rate variation of bright subpulses. In fact, assuming profile variation occurs mainly in the trailing component, the increase of amplitude ratio from 5-min integrations corresponds to a 6 per cent decrease of flux density in the trailing component. Given the average amplitude ratio of 0.18 observed in the detected subpulses and an amplitude ratio of 1 for ordinary integrations, the selected subpulses contribute 6–9 per cent of the flux density in the trailing component. Therefore, if the change of occurrence rate of the selected subpulses were fully responsible for the amplitude-ratio variation, the number of detections around MJD 56257.07 would have dropped by 70–100 per cent, which is clearly not the case. Therefore, it is unlikely that our selected subpulses cause the detected profile variation, which suggests that subpulse variability and integrated profile variation are two different effects. Nevertheless, the analysis is still restricted to roughly the brightest 1 per cent of all single pulses and will be significantly improved by increasing system sensitivity.

3.3 Timing of subpulses

To investigate the impact of subpulses on pulsar timing, we used the subpulses selected in Fig. 7 (3.4 per cent of all periods, from the trailing component, in total approximately 4500 pulses) and compared their timing with ordinary integrations based on all rotations. The TOAs are measured by following the classic template-matching method described in Taylor (1992). The template profile for timing based on subpulses is formed by summing all detected subpulses and performing a Gaussian component smoothing, as in e.g. Kramer (1994). The timing residuals were calculated with the TEMPO2 software package (Hobbs, Edwards & Manchester 2006). Here we used the timing solution obtained from the European Pulsar Timing Array collaboration (Desvignes et al., in preparation), without fitting for any parameters.

In Fig. 15, we present the timing residuals calculated with averages of 30 pulses (not contiguous in time), equivalent to an integration time of 0.5 s. The timing solution has an rms of 4.3 μs, which is greater than the average of the errors owing to white noise (1.6 μs). This suggests the existence of phase jitter. To understand the timing noise better, a standard Kolmogorov–Smirnov (K–S) test has been performed on the TOAs, as in Liu et al. (2012). The measured *p*-value ($\simeq 0.98$) is close to 1, indicating no significant deviation of
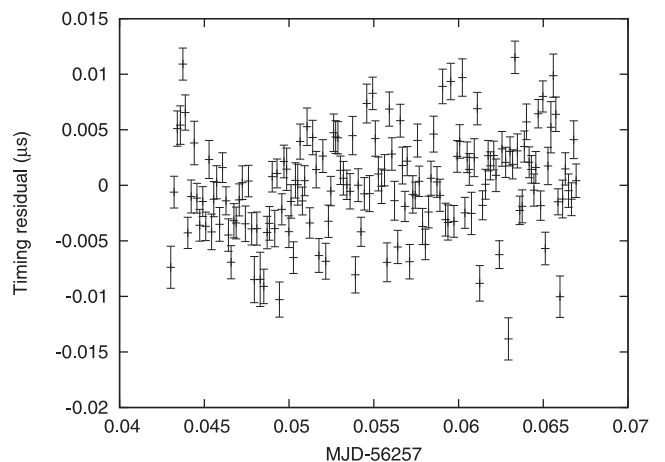

Figure 15. Timing residuals based on 151 averages of 30 subpulses. The rms is 4.3 μs, while the white noise rms indicated from the TOA errors is 1.6 μs.
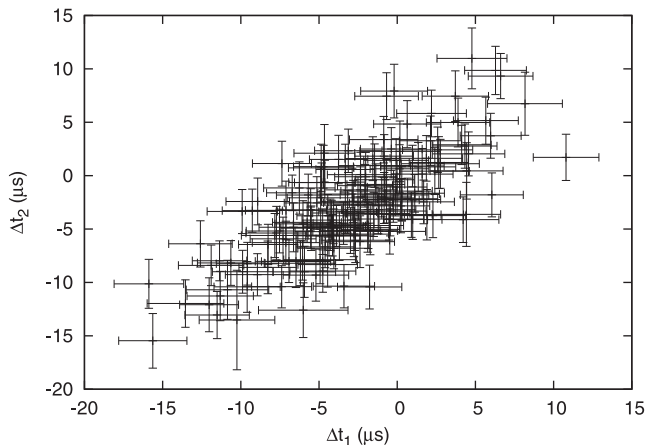
Figure 16. Correlation plot of TOA pairs calculated based on subpulse averages from two individual 80-MHz sub-bands. The data used here are the same as in Fig. 15.
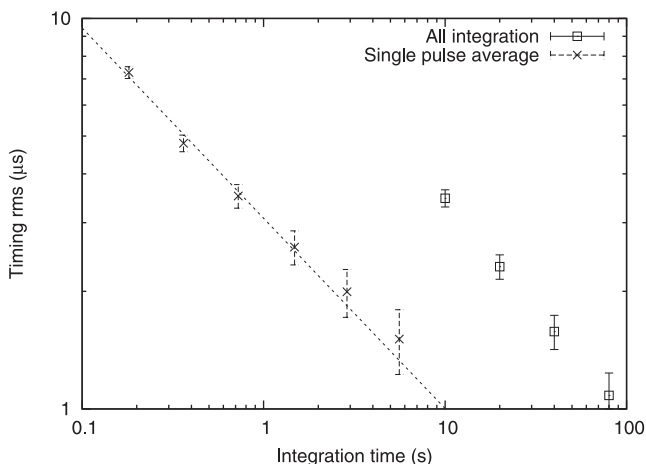

Figure 17. Timing rms of averages based on different numbers of bright subpulses, compared with the rms from integrations of all periods. The dashed line shows a power-law modelling with a fitted index of -0.49 ± 0.02. Note that an integration of 10 s corresponds to roughly 600 pulses.

the residuals from a Gaussian distribution (e.g. Press et al. 1986). In Fig. 16, we divide the entire band into two sub-bands and present a correlation plot of TOAs from them, as in Osłowski et al. (2011) and Shannon & Cordes (2012). The TOA pairs are shown to be highly correlated and the rms of each individual group is also estimated to be roughly equal (4.6 μs), meaning that the noise is correlated and dominated by phase jitter.

In contrast, we did not detect any significant impact of pulse phase jitter on timing with ordinary integrations. Data obtained between MJD 56257.044 and 56257.080, when the observing S/N was maximal, have been examined based on 1-min averages. The resulting timing rms is 1.3 μs, close to the estimated white-noise level (1.1 μs) from the TOA errors. Subtraction of the white-noise contribution from the timing residuals leads to an upper limit of ∼700 ns for jitter noise, based on a 1-min integration time.

In Fig. 17, we present the timing rms values obtained when altering the number of integrated subpulses and compare them with timing rms values yielded by ordinary integrations. It is shown that the jitter noise decreases following the $\sigma_J \propto t_{int}$ law, as expected (Cordes & Shannon 2010), where t_{int} is the integration length of

each average. Averaging 30 subpulses leads to 151 TOAs of rms 4.3 μs. Considering that, during the same period of time, ordinary 1-min integrations lead to 34 TOAs of rms 1.3 μs, timing the averages of subpulses is almost as effective as timing the ordinary integrations ($4.3/\sqrt{151/34} \simeq 2.0$ μs, close to 1.3 μs). Note that only 3.4 per cent of the single rotations were picked up; an improved system sensitivity would enable significantly more subpulse detections. Including those subpulses in timing may significantly decrease the jitter noise and make the timing based on subpulses more efficient (achieving more measurements of the same rms in the same observing time, or equal number of measurements with lower rms) than using all-period integrations. However, this extrapolation is based on the assumption that the subpulses to be included exhibit the same phase jittering as the currently selected ones, which will require further investigation with improved sensitivity to validate it.

4 CONCLUSION AND DISCUSSION

In this article, we have performed a detailed investigation into the profile variation of PSR J1022+1001. Within our 35-h observations, approximately 14 400 subpulses were detected above a 5σ threshold from the WSRT baseband data and most of them are coincident with the trailing component of the integrated profile. The flux densities and polarization properties suggest that they are the bright end of the pulse energy distribution and not a separate population. No giant pulse has been detected. Pulses from the leading and trailing components can happen within the same rotation and their occurrences are shown to be correlated. For pulses from the trailing components, a preferred pulse width of approximately 0.25 ms has been found. Using simultaneous observations at the Effelsberg telescope and the WSRT, we have tracked the variation of integrated profiles on a time-scale of several tens of minutes. Profile instability due to improper polarization calibration and diffractive scintillation was excluded. We have not yet discovered an association between integrated profile instability and subpulse occurrence, possibly owing to the present sensitivity limit. In addition, we have demonstrated the dominance of phase jitter in timing residuals with the subpulse averages from the trailing component and have obtained an upper limit of ∼700 ns for jitter noise based on continuous 1-min integrations. Further investigation with better sensitivity is still required to find out whether timing the averages of subpulses is more efficient than using continuous integrations.

The spin-down power ($\dot{E}$) of PSR J1022+1001 is estimated to be 3.8×10^{32} erg s^{-1} (obtained from the Australia Telescope National Facility (ATNF) Pulsar Catalog, for details see Manchester et al. 2005), significantly less than that of the current few MSPs with giant pulse discoveries (Cognard et al. 1996; Romani & Johnston 2001; Joshi et al. 2004; Knight et al. 2005). Thus, our non-detection of giant pulses from PSR J1022+1001 tends to coincide with the correlation between giant pulse emissivity and spin-down luminosity in MSPs (e.g. Knight et al. 2005). Still, the detected subpulses satisfy the criterion for so-called 'giant micropulses', which requires a peak flux density much greater than 10 times that of the average profile, but an integrated flux density not exceeding 10 times the average (Cairns 2004). Our detection, together with the discovery in PSR J0437−4715 (Jenet et al. 1998), suggests that the emissivity of giant micropulses in MSPs is not necessarily related to the spin-down luminosity. This suggests the possibility that giant micropulses may have a different origin from giant pulses.

The two components of PSR J1022+1001 are separated by only 5 per cent of the period, but have dramatically different emission behaviour. It could be that the two components actually originate

from regions well separated in height, due to the strong winding of the magnetosphere (e.g. Pétri 2011). A fit of the aberration and retardation field-line model to the integrated profile, which estimates the emission latitude, may shed more light on this issue (Dyks, Rudak & Harding 2004).

Admittedly, single-pulse studies of MSPs are still mostly limited by detection sensitivity. With the next generation of radio telescopes, such as the Five-hundred-metre Aperture Spherical Radio Telescope and the Square Kilometre Array, the system sensitivity for pulsar observations will be increased by 1–2 orders of magnitude from the current level (e.g. Liu et al. 2011). This will enable more comprehensive investigations into MSP single pulses, by increasing the number of detections, improving the detection qualities and enabling more case studies. Such efforts would be greatly helpful in understanding the behaviour of single-pulse emission as well as its impact on pulsar timing stability and thus in developing potential approaches to improve timing precision.

REFERENCES

Antoniadis J. et al., 2013, Sci, 340, 448
Cairns I. H., 2004, ApJ, 610, 948
Cognard I., Shrauner J. A., Taylor J. H., Thorsett S. E., 1996, ApJ, 457, 81
Cordes J. M., Lazio T. J. W., 2002, preprint (astro-ph/0207156)
Cordes J. M., Shannon R. M., 2010, preprint (astro-ph/1107.3086)
Demorest P. B., Pennucci T., Ransom S. M., Roberts M. S. E., Hessels J. W. T., 2010, Nat, 467, 1081
Demorest P. B. et al., 2013, ApJ, 762, 94
Dyks J., Rudak B., Harding A. K., 2004, ApJ, 607, 939
Edwards R. T., Stappers B. W., 2003, A&A, 407, 273
Freire P. C. C. et al., 2012, MNRAS, 423, 3328
Hobbs G. B., Edwards R. T., Manchester R. N., 2006, MNRAS, 369, 655
Hotan A. W., Bailes M., Ord S. M., 2004a, MNRAS, 355, 941
Hotan A. W., van Straten W., Manchester R. N., 2004b, Proc. Astron. Soc. Aust., 21, 302
Jenet F. A., Anderson S. B., 1998, PASP, 110, 1467
Jenet F., Anderson S., Kaspi V., Prince T., Unwin S., 1998, ApJ, 498, 365
Jenet F. A., Anderson S. B., Prince T. A., 2001, ApJ, 546, 394
Joshi B. C., Kramer M., Lyne A. G., McLaughlin M. A., Stairs I. H., 2004, in Camilo F., Gaensler B. M., eds, IAU Symp. 218, Young Neutron Stars and Their Environments. Astron. Soc. Pac., San Francisco, p. 319
Karuppusamy R., Stappers B., van Straten W., 2008, PASP, 120, 191
Knight H. S., Bailes M., Manchester R. N., Ord S. M., 2005, ApJ, 625, 951
Kramer M., 1994, A&AS, 107, 527
Kramer M., Stappers B., 2010, in ISKAF2010 Science Meeting
Kramer M., Xilouris K. M., Camilo F., Nice D., Lange C., Backer D. C., Doroshenko O., 1999, ApJ, 520, 324
Kramer M. et al., 2006, Sci, 314, 97

Liu K., Verbiest J. P. W., Kramer M., Stappers B. W., van Straten W., Cordes J. M., 2011, MNRAS, 417, 2916
Liu K., Keane E. F., Lee K. J., Kramer M., Cordes J. M., Purver M. B., 2012, MNRAS, 420, 361
Manchester R. N., 2013, Class. Quant Grav., 30, 224010
Manchester R. N., Hobbs G. B., Teoh A., Hobbs M., 2005, AJ, 129, 1993
Ord S. M., van Straten W., Hotan A. W., Bailes M., 2004, MNRAS, 352, 804
Osłowski S., van Straten W., Hobbs G. B., Bailes M., Demorest P., 2011, MNRAS, 418, 1258
Osłowski S., van Straten W., Demorest P., Bailes M., 2013, MNRAS, 430, 416
Osłowski S., van Straten W., Bailes M., Jameson A., Hobbs G., 2014, MNRAS, 441, 3148
Özel F., Psaltis D., Ransom S., Demorest P., Alford M., 2010, ApJ, 724, L199
Pétri J., 2011, MNRAS, 412, 1870
Press W. H., Flannery B. P., Teukolsky S. A., Vetterling W. T., 1986, Numerical Recipes: The Art of Scientific Computing. Cambridge Univ. Press, Cambridge
Purver M. B., 2010, PhD thesis, Univ. Manchester
Ramachandran R., Kramer M., 2003, A&A, 407, 1085
Romani R., Johnston S., 2001, ApJ, 557, L93
Shannon R. M., Cordes J. M., 2012, ApJ, 761, 64
Shannon R. M. et al., 2013, Sci, 342, 334
Stairs I. H., Thorsett S. E., Camilo F., 1999, ApJS, 123, 627
Taylor J. H., 1992, Phil. Trans. R. Soc. A, 341, 117
van Haasteren R. et al., 2011, MNRAS, 414, 3117
van Straten W., 2004, ApJ, 152, 129
van Straten W., 2006, ApJ, 642, 1004
van Straten W., 2013, ApJS, 204, 13
van Straten W., Bailes M., 2011, Proc. Astron. Soc. Aust., 28, 1
Verbiest J. P. W. et al., 2009, MNRAS, 400, 951
Weltevrede P., Wright G., Johnston S., 2012, MNRAS, 424, 843
Yardley D. R. B. et al., 2011, MNRAS, 414, 1777
You X.-P. et al., 2007, MNRAS, 378, 493

APPENDIX A: EXAMPLE OF CORRUPTED DATA DUE TO FAULTY POWER LEVEL SETTING

The data from the failed observing session at MJD 55974 at the Effelsberg telescope provide insights into the effect of two-bit sampling on profile evolution. In this observing run, the signal level attenuator was inadvertently set too high, resulting in voltages that were too small as input to the eight-bit analogue-to-digital converter (ADC) and reducing it to a low-bit (two-bit or even smaller) system. These data allow us to assess the effect of low-bit sampling on PSR J1022+1001's profile shape variation, thus highlighting an extreme case of signal clipping.

Fig. A1 shows a grey-scale image of the profile as a function of frequency before dedispersion. Within each 25-MHz sub-band, there is negative power distributed in a similar fashion to that shown by fig. 4 of Jenet & Anderson (1998), which is a consequence of low-bit sampling. As the pulsar signal is dedispersed, the negative dip, which would suppress the power of the signal, leads the profile at lower frequencies and trails at higher ones. This will result in additional peak amplitude ratio variation across the sub-band, which can be witnessed in Fig. A2. Here, the profile from the lower side of a sub-band exhibits a significantly suppressed first component, while that from the upper side is affected mostly at the phase of the trailing component.

Fig. A3 shows the polarization profile of data in Fig. A1. It can be seen that the linear and circular components retain their original shape in general, while the total intensity profile is greatly
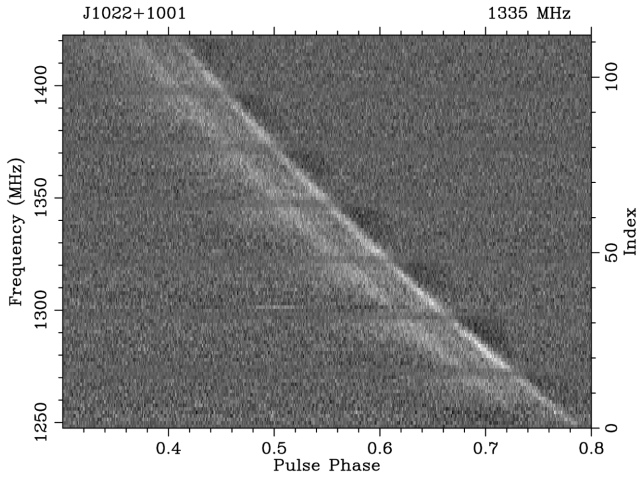
Figure A1. Grey-scale image of the profile against frequency obtained from Effelsberg at MJD 55974 with 4-h integration time.
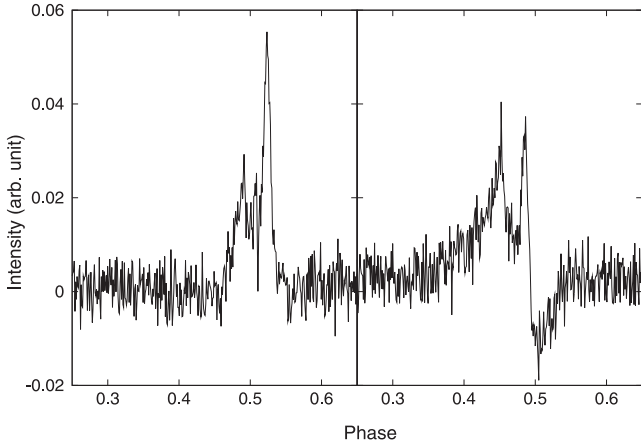

Figure A2. Pulse profiles formed with a bandwidth of 3 MHz on the lower (left) and upper (right) sides of the 1285-MHz sub-band, respectively, from the data shown in Fig. A1. The central frequencies are 1277 and 1293 MHz, respectively.
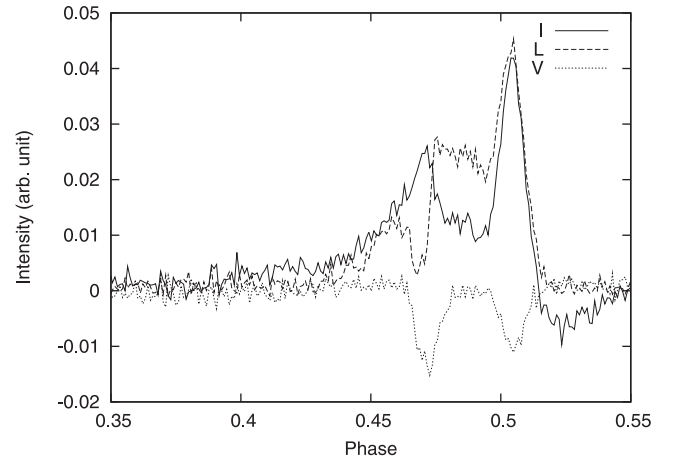

Figure A3. Polarization profile of the data in Fig. A1, averaging over all frequencies.

suppressed and lower than the linear component for most of the on-pulse phases, including the valley region between the two main peaks. This explains why the WSRT profile shown in Fig. 1 is slightly overpolarized.

This paper has been typeset from a TEX/LATEX file prepared by the author.